Chapter

Nanostructure Technology for EO/IR Detector Applications

Ashok K. Sood, John W. Zeller, Gopal G. Pethuraja, Roger E. Welser, Nibir K. Dhar and Priyalal S. Wijewarnasuriya

Abstract

This chapter covers recent advances in the development of nanostructure-based material technologies to benefit next-generation electro-optical (EO) and infrared (IR) sensor and imager applications. Nanostructured materials can now be integrated into a variety of technological platforms, offering novel optoelectrical properties that greatly enhance device performance in many practical applications. Use of novel carbon nanotube (CNT) based materials has enabled new approaches for applying nanostructure design methodologies that can offer enhanced performance for low-cost bolometers for IR detection and imaging applications. We will discuss the development of carbon nanostructure based infrared detectors and arrays, including concepts that will provide high performance, high frame rate, and uncooled microbolometers for mid-wave infrared (MWIR) and long-wave infrared (LWIR) band detection. In addition, nanostructured antireflection (AR) coatings are being developed that significantly enhance transmission over a broad spectrum, providing substantial improvements in device performance compared to conventional thin film AR coatings. These nanostructured AR coatings have been demonstrated over visible to LWIR spectral bands on various substrates. In this chapter, we discuss both theoretical and measured results of these diverse nanostructure technologies to advance sensing performance over a wide range of spectral bands for defense, space, and commercial applications.

Keywords: sensors, detectors, infrared, electro-optical, carbon nanotubes nanostructures, antireflection coatings

1. Introduction

Nanostructures come in many different physical forms having varied and diverse optoelectronic properties that enable them to benefit many different applications, of which electro-optic/infrared (EO/IR) detectors and systems may be considered in the forefront. Rapid advances in these technologies that have recently taken place are enabling the development of more capable sensing and imaging systems and subsystems with notable improvements in performance. Such nanostructure-based devices and systems operating from the visible to long-wave infrared (LWIR) portions of the electromagnetic spectrum have been and continue to be developed for use in a variety of defense and commercial applications [1, 2].

Detectors and imaging arrays operating over the visible spectrum (~400–700 nm) are mostly Si-based, consisting of charge-coupled device (CCD) imagers and complementary metal oxide semiconductor (CMOS) technologies. For detection of infrared (IR) wavelengths invisible to the human eye, which span the range of approximately 1.0 μm in the near-infrared (NIR) to beyond 30 μm, other materials and technologies are required [3].

The IR spectrum is categorized based primarily on the spectral locations of atmospheric transmission windows (**Figure 1**). IR radiation falling within these bands can generally be transmitted and/or received with relatively low attenuation. The NIR and short-wave infrared (SWIR) bands (~0.8–2.5 μm) like the visible mostly involve reflected light, for which materials including InGaAs, InP, and Ge are used for detection and imaging. For the mid-wave infrared (MWIR: 3–5 μm) and LWIR (8–14 μm) wavebands, which conversely involve detection of objects emitting thermal radiation, HgCdTe and InSb based focal plane arrays (FPAs), strained-layer superlattice (SLS) structures, and microbolometers (e.g., Si-MEMS devices) have been and are being utilized [4].

Uncooled microbolometers used as detectors in thermal cameras have traditionally been based on silicon as well as vanadium oxide material deposited on silicon. However, the use of novel carbon nanotube-based detector elements in IR microbolometer pixels is attractive due to the potential for high electron mobilities and high temperature sensitivity [5]. Carbon nanotubes (CNTs) basically comprise hexagonal sheets of graphene, a material with enhanced electrical capabilities, rolled into cylinders that exhibit exceptional conductivity and strength [6].

In following sections of this chapter, we discuss integration of CNTs in detector elements for next-generation high performance, high frame rate, and uncooled bolometer arrays that can provide enhanced sensitivity for MWIR and LWIR band detection and imaging [7, 8].

Sensors and detector arrays generally comprise semiconductor materials characterized by high refractive indexes, which results in significant optical reflection from the top surface that reduces light throughput into and thus light absorbed by the detector. To address this, nanostructured antireflection (AR) coatings have been developed to reduce unwanted reflections and increase the transmission of light from visible to LWIR wavelengths, thereby improving detector performance [9, 10].

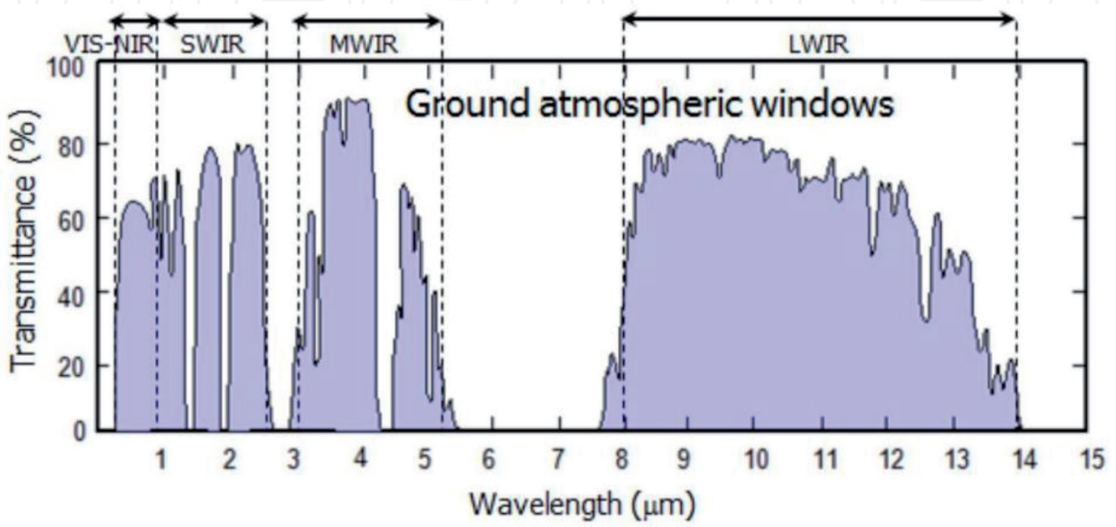

Figure 1.
IR spectral band atmospheric windows [3].

We likewise discuss in this chapter the growth processes, performance, and device applications of these advanced nanostructured AR coatings capable of minimizing reflection losses over a wide range of wavelengths and incident angles.

2. Carbon nanotube-based microbolometers for IR imaging

2.1 Properties and applications of carbon nanotubes

Graphene is a two-dimensional analogue of carbon-based graphite material that has exceptional electrical characteristics, e.g., mobilities up to 15,000–200,000 cm^2/Vs, derived from the bonding characteristics of the carbon sheets [5].

There are multiple pathways for creating graphene sheets, which include: exfoliation, unzipping through etching, growth from sublimation, and epitaxial growth from a catalyst layer [11]. The absence of a band gap in graphene limits voltage and power gains that may be achieved through operation of a device in the saturation regime. To overcome this, several doping strategies as shown in **Figure 2** have been proposed and tested, including: electrostatic doping, chemical doping, and stress or geometry restricted doping by breaking the graphene periodicity [5, 11]. Since it can be doped electrostatically, graphene provides a useful solution for certain electronic applications such the channels in field effect transistors (FETs) [12].

Carbon nanotubes (CNTs), which like graphene are allotropes of carbon, may be considered formed of hexagonal sheets of graphene rolled into cylinders (**Figure 3**). CNTs exhibit bandgaps in the range of zero to ~2 eV, and demonstrate metallic or semiconducting behavior depending mainly on their diameter and orientation of the hexagonal graphene structure along the axis of the tube (armchair, zigzag, or

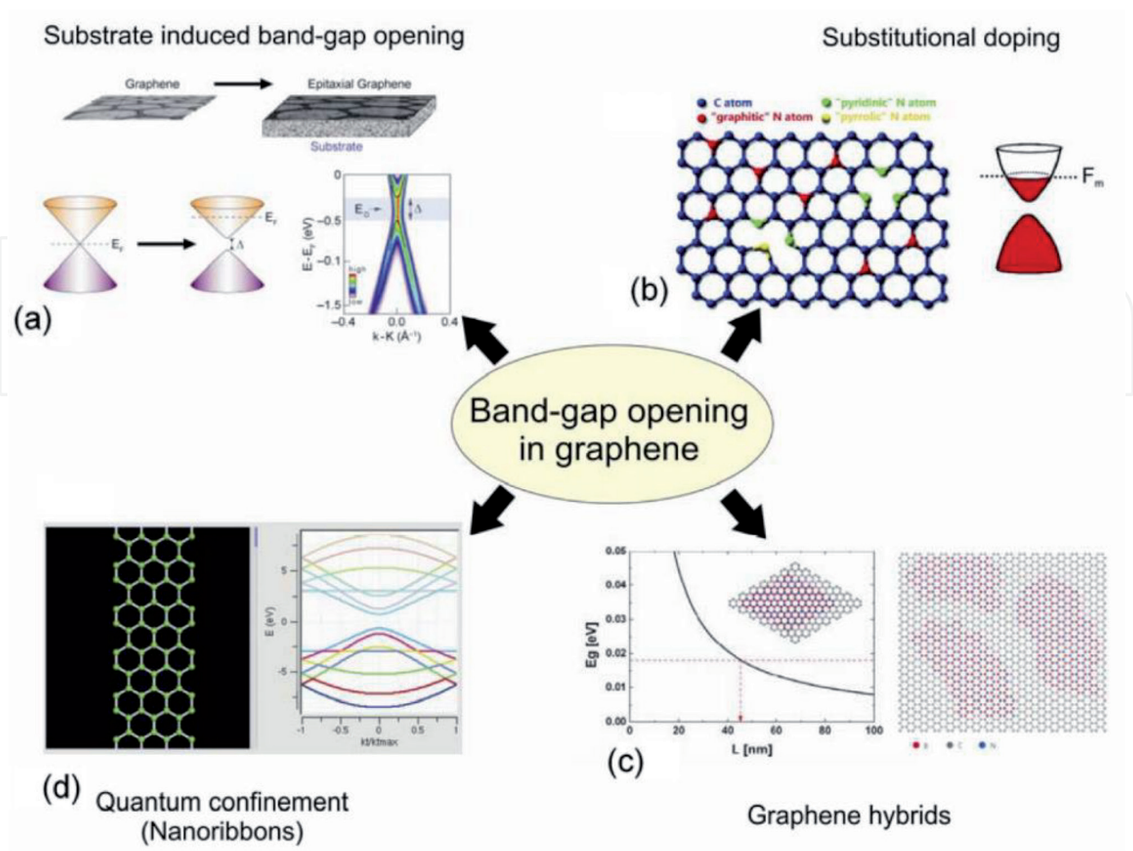

Figure 2.
Diagram showing multiple mechanisms for inducing a band gap in graphene [5, 11].

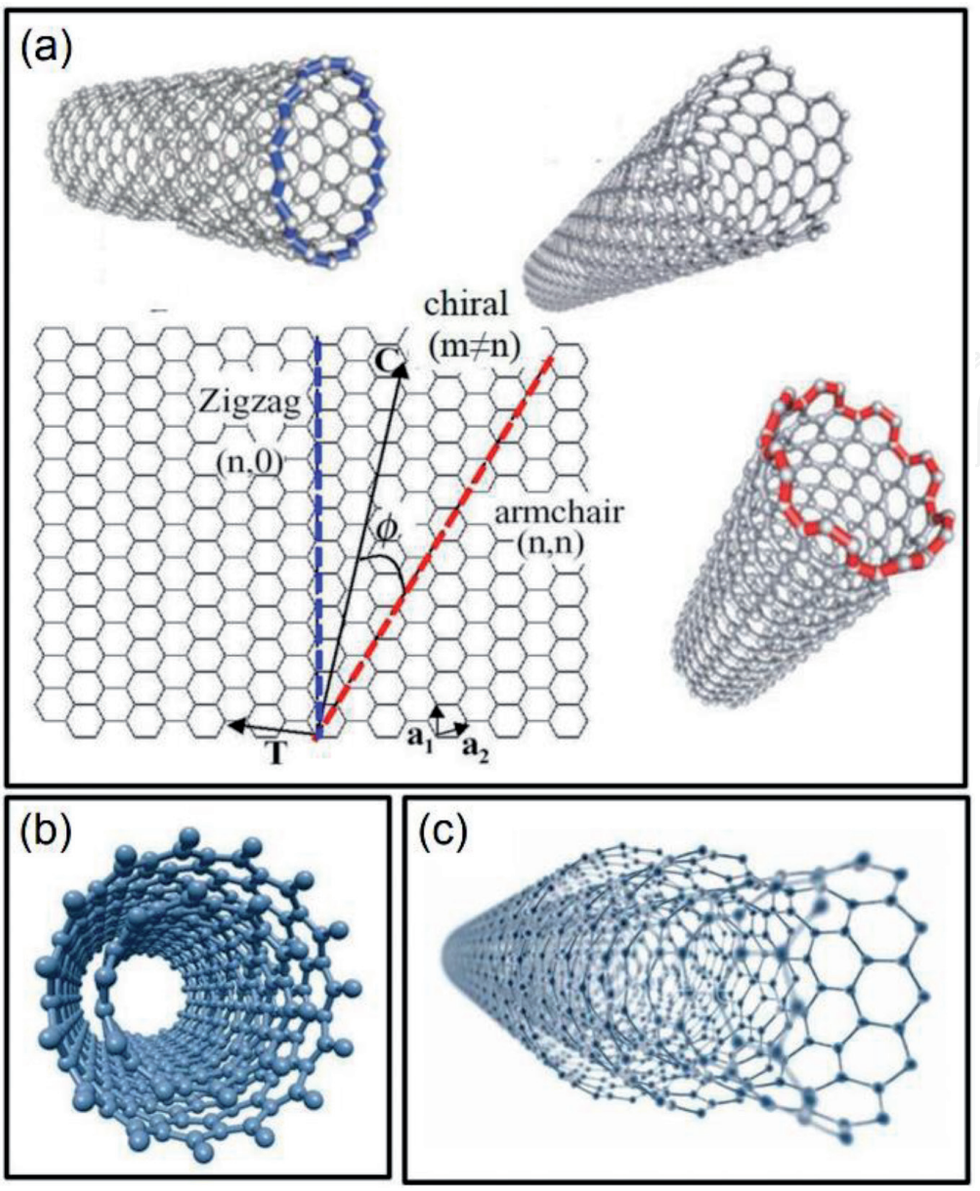

Figure 3.
Structural models of carbon nanotubes categorized based on the number of walls. (a) SWCNTs structures based on their chirality (zigzag, armchair, and chiral). (b) Structure of MWCNTs made up of two concentric shells. (c) MWCNTs composed of many overlapping shells [13].

chiral) as illustrated in **Figure 3(a)** [13]. CNTs can exhibit exceptional conductivity, and as a result have found application in nanoscale FETs that have enabled novel devices including intermolecular logic gates [5].

CNTs fall under two main categories: single-walled carbon nanotubes (SWCNTs), like those shown in **Figure 3(a)**, and multiwalled carbon nanotubes (MWCNTs), depicted in **Figure 3(b)** and **(c)** [14]. As their names suggest, SWCNTs comprise single sheets of graphene for the outer walls, while MWCNTs are composed of multiple overlapping sheets of graphene rolled up in cylindrical forms. The lengths of SWCNTs are usually in the 50–300 nm range (though up to centimeter lengths are possible) with typical diameters of 1–2 nm, while diameters of MWCNTs can exceed 100 nm [13].

2.2 Designing optimal microbolometer elements with CNTs

The novel application we are considering involves using CNT materials in the design of bolometer elements for MWIR and LWIR band detection and imaging.

These pixel elements are fabricated above the CMOS readout circuit unit cells. The focus will be on the development of relatively small (5–10 μm) bolometer unit cells with enhanced temperature coefficients of resistance (TCRs) and frequency response in the 1–10 kHz range. The feasibility of such arrays makes possible a significant number of defense and commercial applications involving uncooled IR detection and imaging.

2.2.1 Photon- vs. thermal-based detectors

Detectors of IR radiation can be generally separated into two distinct categories: photon-based and thermal-based detectors [15, 16]. Photon-based detectors involve the absorption of incident photons as governed by the bandgap of the detector material, where the absorbed photons create electron-hole pairs that produce a photocurrent. Photon detectors may be further classified as p-n junction detectors, avalanche photodiodes, photoconductors, and Schottky diodes. Photon-based IR absorbers have a fast absorption response, but typically require cooling due to thermal effects.

Thermal-based IR detectors, though normally characterized by a much slower absorption response, commonly operate at room temperature and typically have higher responsivities at longer (e.g., IR band) wavelengths [15]. In such devices, the absorption of incident IR radiation raises the temperature of the material. In pyrometers, this is achieved through changes in electrical polarization, while in bolometers by changes in the resistance of the absorbing material. Through incorporating CNT absorbing material into bolometer pixel elements these temperature-based resistance changes may be further enhanced, thereby enabling improved detection and imaging capabilities.

2.2.2 Temperature coefficient of resistance

The temperature that a bolometer pixel reaches after exposure to IR radiation can be determined by measuring its electrical resistance. This in turn may be achieved by comparing this resistance to a lookup table, or by using knowledge of the temperature coefficient of resistance (TCR). A large TCR, which corresponds to a higher thermal resistance that results in a larger rise in temperature, is desirable for achieving greater temperature resolution.

The TCR of a material is defined as the change in electrical resistance per degree Kelvin divided by the absolute electrical resistance measured at the quiescent point:

$$TCR = \frac{1}{R_e}\frac{dR_e}{dT} \tag{1}$$

The electrical resistance of a pixel after it reaches a temperature ΔT above its ambient becomes:

$$R_e(T) = R_e(T_0)(1 + TCR) \tag{2}$$

From this relationship, the pixel temperature may be calculated.

2.2.3 CNTs as bolometric elements

Microbolometers are specific types of bolometers used as detectors in thermal cameras that have traditionally been based on vanadium oxide (VOx) or amorphous

silicon material on silicon. Using carbon-based CNT detector elements in IR microbolometer pixels is attractive due to their high mobility, large thermal resistance, and intrinsically high TCR values [4]. The high thermal conductivity, high strength, and other optical and electrical properties of CNTs that can be varied over a wide spectral range likewise contribute towards their usefulness in this application.

The low electrical resistance and corresponding high conductivity of CNTs are mainly attributed to electrons tunneling between adjacent nanotubes and corresponding unimpeded flow of electrical current. The tunnel barrier height between the CNTs directly impacts the amount of heating that takes place for a given electric field. Assuming that electrons can transport across it, this barrier is governed by Fowler-Nordheim-type tunneling or thermionic emission. The expected associated TCR values can be calculated using the following expression:

$$I = q \int_0^\infty T_t(E) v(E) DOS(E) f(E,T) dE \tag{3}$$

where T_t, v, DOS, and f are the transmission coefficient, thermal velocity, density of states, and distribution function, respectively, for electrons in the CNT. We have performed this calculation of TCR and current as a function of barrier height and electric field, and these results are shown in **Figure 4** [16].

The theoretical TCR values for a CNT film are plotted in **Figure 4(a)** as a function of the electric field between the nanotubes and the barrier height. The calculations predict a comparatively very large TCR, which can be attributed to the relatively large barrier height between adjacent SWCNTs. If a relatively low barrier height on the order of 0.06 eV is assumed, then a TCR of approximately 2.5% is obtained. It is noted that a TCR of this magnitude is associated with very low output currents. **Figure 4(b)** shows the plotted bolometer current density as a function of barrier height and electric field.

Research on this CNT absorber material has provided proof-of-principle demonstrations of extraordinary TCRs in devices [7]. Within the temperature region where the composite material undergoes a volume phase transition, considerable changes in resistance are observed. Negative TCRs of magnitude larger than −10%/°C were determined, and other composite structures with thinner suspended

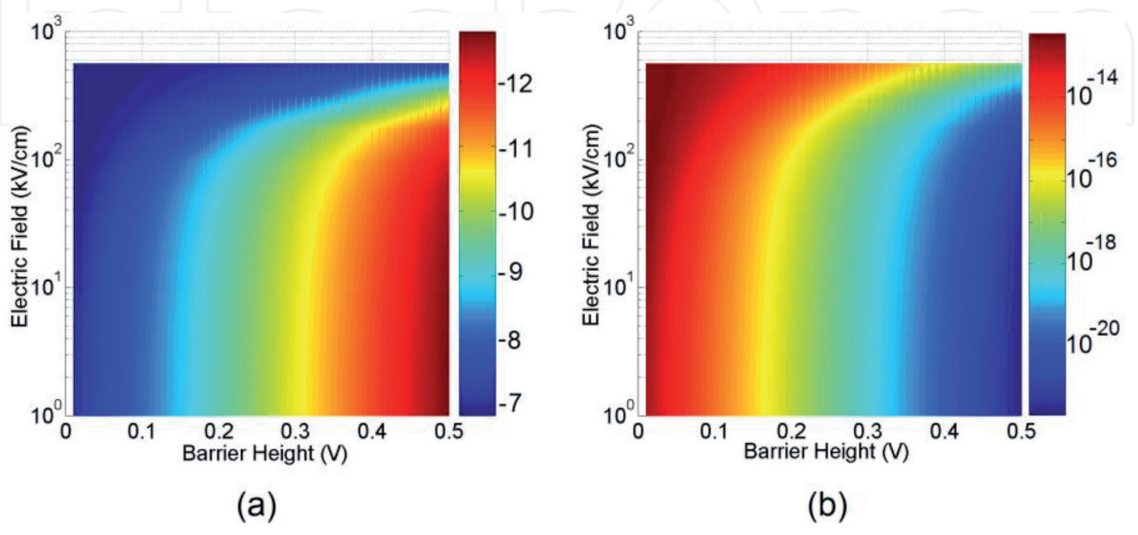

Figure 4.
(a) Contour plot of TCR vs. electric field and barrier height between SWCNTs of the film (color bar scale in units of %TCR); (b) bolometer current as a function of electric field and barrier height (color bars scale in units of amperes) [16].

films achieved TCRs in excess of −50%/°C. Such high TCR values enable up to a threefold enhancement in detector responsivity.

2.3 Model for CNT-based IR bolometers

This section includes an assessment of the design of bolometer elements using carbon nanotubes as both the IR absorbing material and electrical response material [14]. The aim is to first determine the thermal response of the bolometer absorber, and then establish how the electrical characteristics of the CNT material are altered by changes in temperature following IR absorption. Here the focus is on an absorbing material composed of a CNT film comprising randomly situated CNTs each of 2 nm thickness.

2.3.1 Heat flow equation

To determine the temperature of the material in the presence of IR radiation, we start with the heat flow equation. This partial differential equation relates the time rate of change in temperature to the position and the rate of net heat that is absorbed by the material as a function of time and position:

$$C_v \frac{\partial T}{\partial t} = \kappa \nabla^2 T + H_{net} \tag{4}$$

where C_v is the thermal capacitance (J/K cm^3), κ is the thermal diffusion coefficient (W/K cm), and H_{net} is the net power absorbed by the material (W/cm^3). To solve this equation for the CNT bolometer, we must first determine C_v and κ for the CNT and CNT film.

2.3.2 Thermal capacitance of CNT absorber

To determine the heat capacity of a carbon nanotube, we first determine the internal vibrational energy of the CNT, and then take the derivative with respect to temperature. The internal energy is found by calculating the energy of each vibrational mode, multiplying by the probability that the mode is populated using Bose-Einstein statistics, and then summing over all the allowed modes.

Since the number of allowed modes is dependent on the diameter and wrapping angle of the CNTs, we must take a statistical sample. After multiplying the heat capacity of the individual CNTs by the number of CNTs in the film to provide a reasonable value for the heat capacity of the film, and inserting numerical values for physical constants, we arrive at the following average numerical value for the thermal capacity of a CNT:

$$C_{vt} \approx 1.4 \times 10^{-18} Ld \tag{5}$$

where L is the CNT length in microns and d is the CNT diameter in nanometers.

2.3.3 CNT thermal diffusion coefficient

In addition to the thermal capacitance, we need to determine the thermal diffusion coefficient and then the thermal resistance of a single CNT. Experiments on isolated CNTs have involved fitting the coefficient of thermal diffusion to data, obtaining the following expression [16]:

$$\kappa(L,T) = \left[3.7 \times 10^{-7} T + 9.7 \times 10^{-10} T^2 + \frac{9.3}{T^2}\left(1 + \frac{0.5}{L}\right)\right]^{-1} \quad (6)$$

From κ we can obtain the thermal resistance R_T of a single CNT using the following definition:

$$R_T = \frac{4L}{\kappa \pi d^2} \quad (7)$$

Using typical values for a CNT gives the following numerical value for its thermal resistance:

$$R_T \approx 5 \times 10^8 (L/d^2) \quad (8)$$

where R_T is in units of K/W. Thus, a CNT that is 1 μm long and 1 nm in diameter will have a thermal resistance of ~5×10^8 K/W.

2.3.4 Net IR radiation power absorbed

Now that the thermal diffusion and capacitance are known, to begin solving the above heat flow equation in order to determine the bolometer temperature we first need to determine the net IR power absorbed by the bolometer, H_{net}. This parameter can be established using the Stefan-Boltzmann law for blackbody radiation, which relates the net power absorbed to the temperatures of the subject and of the bolometer using the following expression:

$$H_{net} = \sigma A \varepsilon \left(T_{obj}^4 - T_b^4\right) \quad (9)$$

where σ, A, ε, T_{obj} and T_b are the Stefan-Boltzmann constant, cross-sectional area, emissivity, object of interest temperature, and bolometer absorber temperature, respectively. **Figure 5** shows the net IR power absorbed by the absorber material as a function of bolometer temperature for objects radiating at 20.0°C and

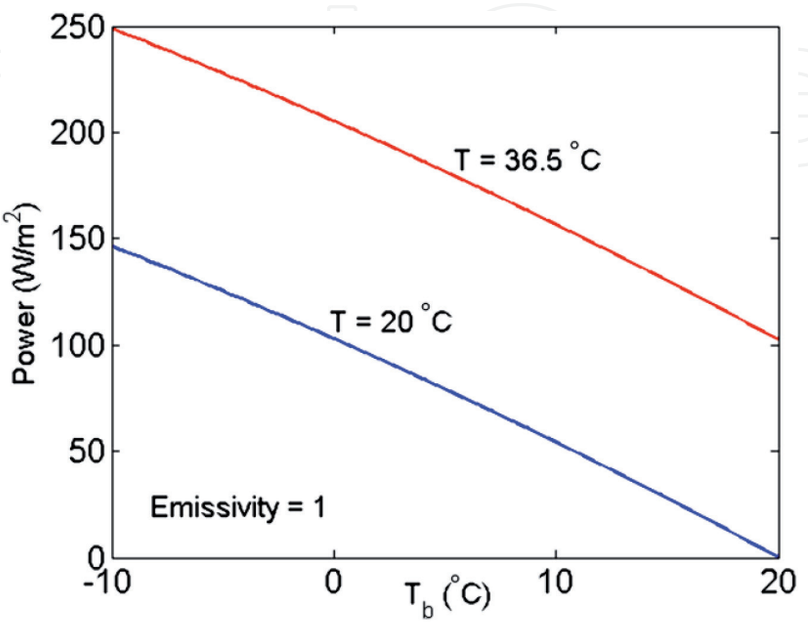

Figure 5.
Net power received by bolometer as a function of bolometer temperature [16].

36.5°C [16]. Cooling the bolometer down to 30°C below room temperature enables significantly more power to be absorbed, which can lead to a much stronger signal.

2.3.5 Calculating the bolometer temperature distribution

Using the above expressions for C_{vt}, κ, and H_{net}, we can convert the heat flow equation above into a thermal network like that illustrated in **Figure 6** [14]. Each resistor in the figure represents the thermal resistance of the CNTs in series with the thermal resistance between adjacent CNTs. The capacitors represent the thermal capacity of the individual CNTs, while the current sources represent the net IR radiation absorbed by each CNT.

This thermal network contains thousands of nodes, where there is a specific equation relating the thermal resistance, capacitance, and net power for each node. This system of equations can be solved to determine the temperature as a function of position and time throughout the bolometer absorber.

The output data from these calculations are shown plotted in **Figure 7** for different CNT network types [16]. Here, we assume the pixel tightly packed with CNTs and H_{net} of 1 nW. Two different thermal resistance values were modeled for the nanotubes: 5×10^8 K/W and 1×10^9 K/W, shown in **Figure 7(a)** and **(b)**, respectively.

As expected, a higher thermal resistance results in a greater temperature difference from the ambient. We note that in general the thermal resistance also rises with increasing temperature, resulting in further heating of hot spots. The color-mapped temperature gradients of the contact legs that connect the film to the readout integrated circuit (ROIC) can be clearly seen in **Figure 7**.

2.4 CNT-based microbolometer pixels

Networks of SWCNTs are considered as potential replacements for VOx and amorphous silicon in uncooled microbolometer-based infrared focal plane arrays

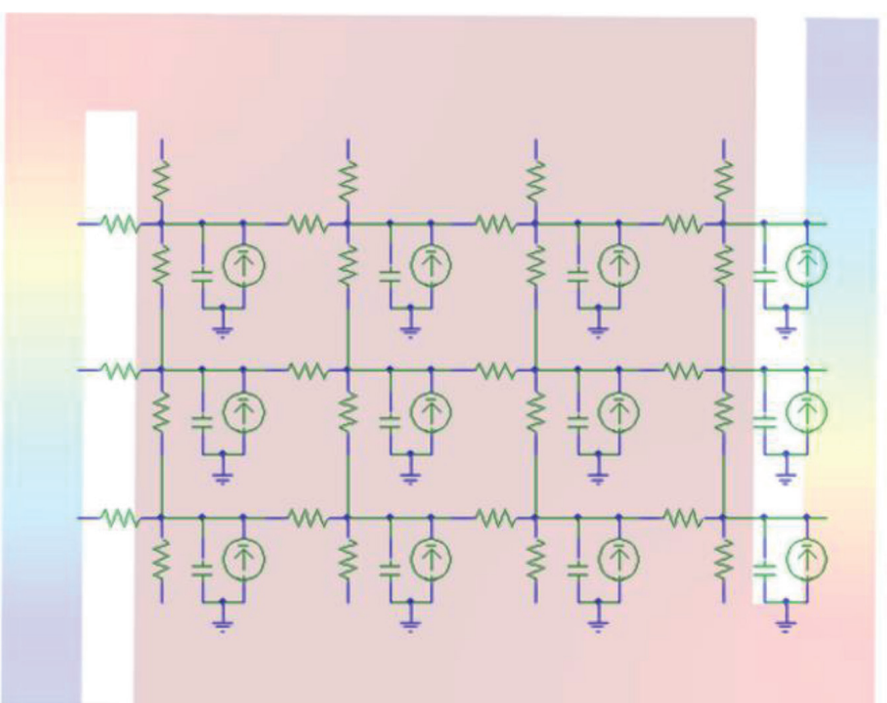

Figure 6.
Schematic of superimposed thermal network for calculating temperature map of CNT-based bolometer absorber [14].

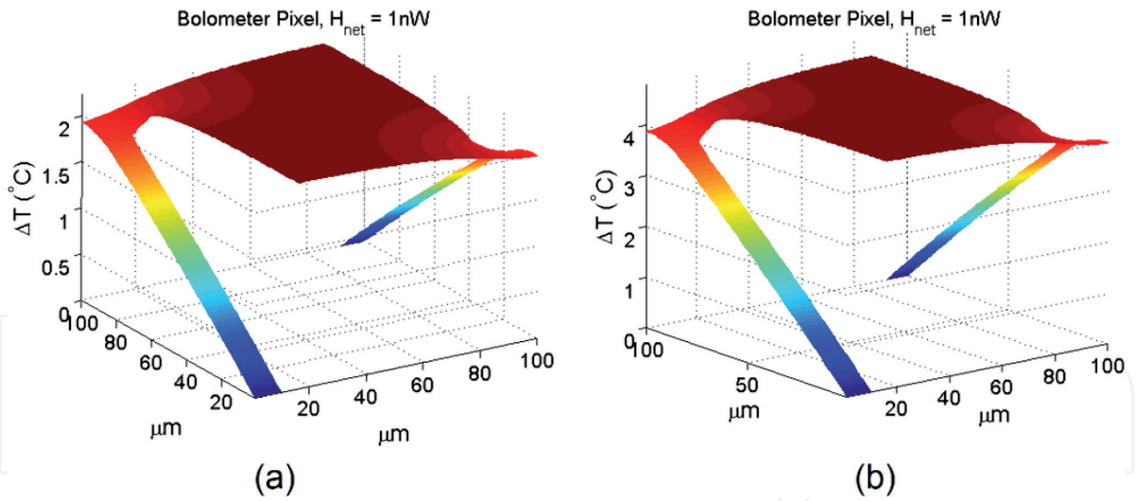

Figure 7.
Temperature map of bolometer pixel when net absorbed power H_{net} is 1 nW, and CNT thermal resistance is (a) 5 × 10^8 K/W and (b) 1 × 10^9 K/W. The pixel is assumed to be tightly packed with CNTs [16].

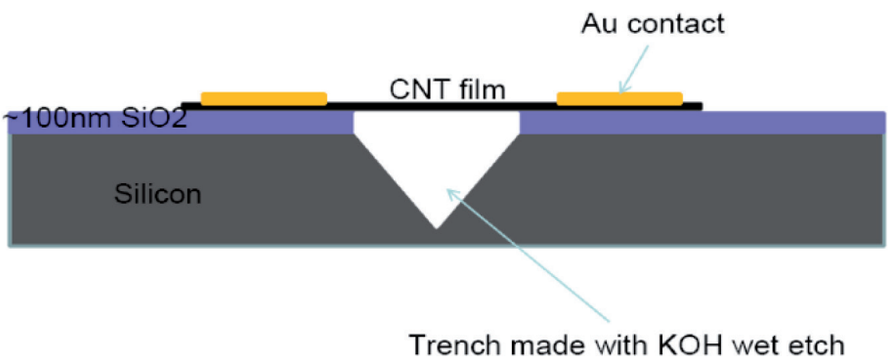

Figure 8.
CNT bolometer test fixture to evaluate CNT film quality [14].

(IRFPAs). These SWCNT-based microbolometer pixels can be fabricated on top of the CMOS readout circuit unit cell. Several potential benefits of SWCNTs over existing state-of-the-art films include low thermal mass, high absorption coefficients in the IR, and TCRs greater than 4%/K.

Another benefit of utilizing SWCNTs involves their compatibility with CMOS wafer processes, which can enable cost-effective manufacturing for uncooled IRFPAs. SWCNTs suspended in either aqueous solutions or other solvents may be applied uniformly to a silicon wafer using standard wafer fabrication equipment. Once this process is optimized, the back end of line (BEOL) standard CMOS process can be modified to continue processing SWCNT microbolometers.

The adaption of SWCNTs to CMOS process technologies has demonstrated the potential for very small pixel sizes with sufficient yields [13]. In addition, there is evidence that unlike devices using VOx and amorphous Si, SWCNT-based microbolometers are not limited in performance due to the 1/*f* noise floor [14].

Optimization of the growth of SWCNTs and MWCNTs has been performed. Grown CNTs have been shown to be easily separable from the growth substrate. Good length/diameter uniformity has also been demonstrated. **Figure 8** shows the fixture used to evaluate the CNT films for bolometric applications [14]. This fixture was employed for evaluation of the optoelectronic characteristics of the CNT samples.

In addition, preliminary TCR measurements have been carried out with CNT materials, examples of which are shown in **Figure 9**. **Figure 9(a)** shows a scanning

electron microscopy (SEM) image of representative MWCNT films in unsuspended and suspended forms, respectively [17]. Unlike their SWCNT counterparts, the MWCNT films leave substantial portions of the substrate uncovered. In addition, some minor recess deformation is visible on the suspended MWCNT films, which are in the same thickness range as the SWCNT films.

In **Figure 9(b)**, a transmission electron microscopy (TEM) image of an individual representative MWCNT is shown. This MWCNT has a large hollow center ~10 nm in diameter and contains approximately 40–50 shells. **Figure 9(c)** presents the dense "forest-like" growth of oriented MWCNTs with good length/diameter uniformity [16]. Here the CNT growth is easily distinguishable from the substrate.

All the MWCNT films studied show semiconductive resistance-temperature (R-T) behavior characterized by the representative curve depicted in **Figure 10** [17]. It is seen that the increase in resistivity of the MWCNT films with decreasing temperature is much less than that of the SWCNT films, which is not unexpected considering the much smaller bandgap of MWCNTs. This reduced temperature dependence implies smaller absolute TCR values for the MWCNTs. For example, the absolute TCR value at room temperature for the MWCNT films is about 0.07%/K, in contrast to 0.17%/K for the SWCNT films.

Two notable differences are discernable between the MWCNT and SWCNT films: the former have significantly higher $\Delta R/R_0$ and much shorter response times compared to the latter. The $\Delta R/R_0$ for MWCNT samples is typically in the range of a few percent, which is above an order of magnitude higher than that of SWCNT films suspended in an aqueous solution and two orders of magnitude higher than that of unsuspended SWCNT films at comparable IR power.

Figure 11 compares the photoresponse R/R_0 of MWCNT films in unsuspended and suspended cases, where R_0 is the sample resistance before IR radiation was turned on and the change in the resistance ΔR caused by IR radiation is given as $R–R_0$. Physical suspension of the MWCNT films (**Figure 11(b)**) and SWCNT films (**Figure 11(d)**) leads to further improvement in R/R_0 compared to that of their unsuspended counterparts in **Figure 11(a)** and **(c)**, respectively [2]. Considering the lower absolute TCR values of MWCNTs, the much enhanced photoresponse of these MWCNT films can be attributed to the naturally suspended inner CNT shells, which may provide an ideal configuration to enhance the bolometric effect by improving light absorption and reducing thermal transfer.

Carbon nanotubes as absorbing materials in microbolometers show much promise for providing greater TCR values, and thus improved IR detection and imaging performance. Nevertheless, additional work is needed in the development, testing, and optimization of microbolometer arrays that can offer superior performance to current well-established Si- and VOx-based technologies. The other nanostructure

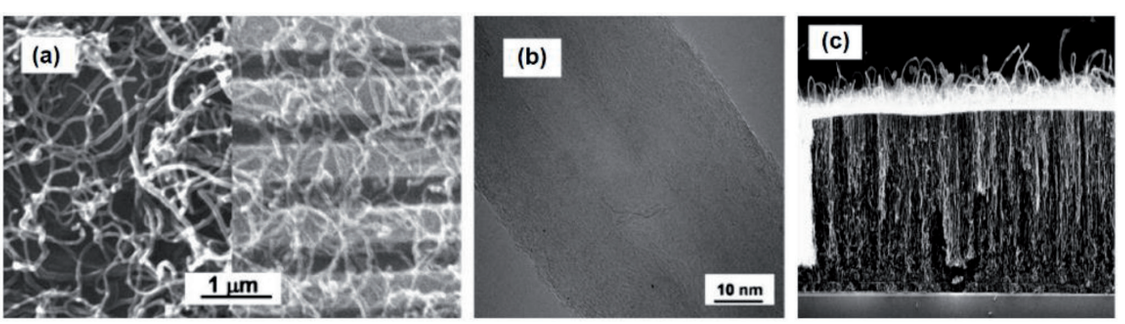

Figure 9.
(a) SEM images of unsuspended (left) and suspended (right) MWCNT films. (b) TEM image of a representative MWCNT, for which the shell number is estimated to be in the range of 40–50 [17]. (c) Dense oriented MWCNT growth [16].

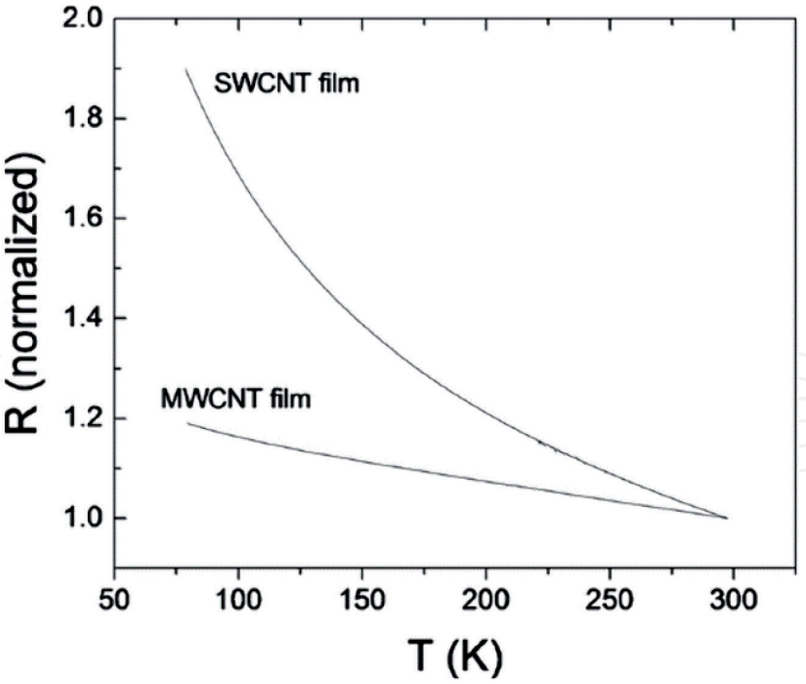

Figure 10.
Resistance vs. temperature curves for SWCNT and MWCNT films [17].

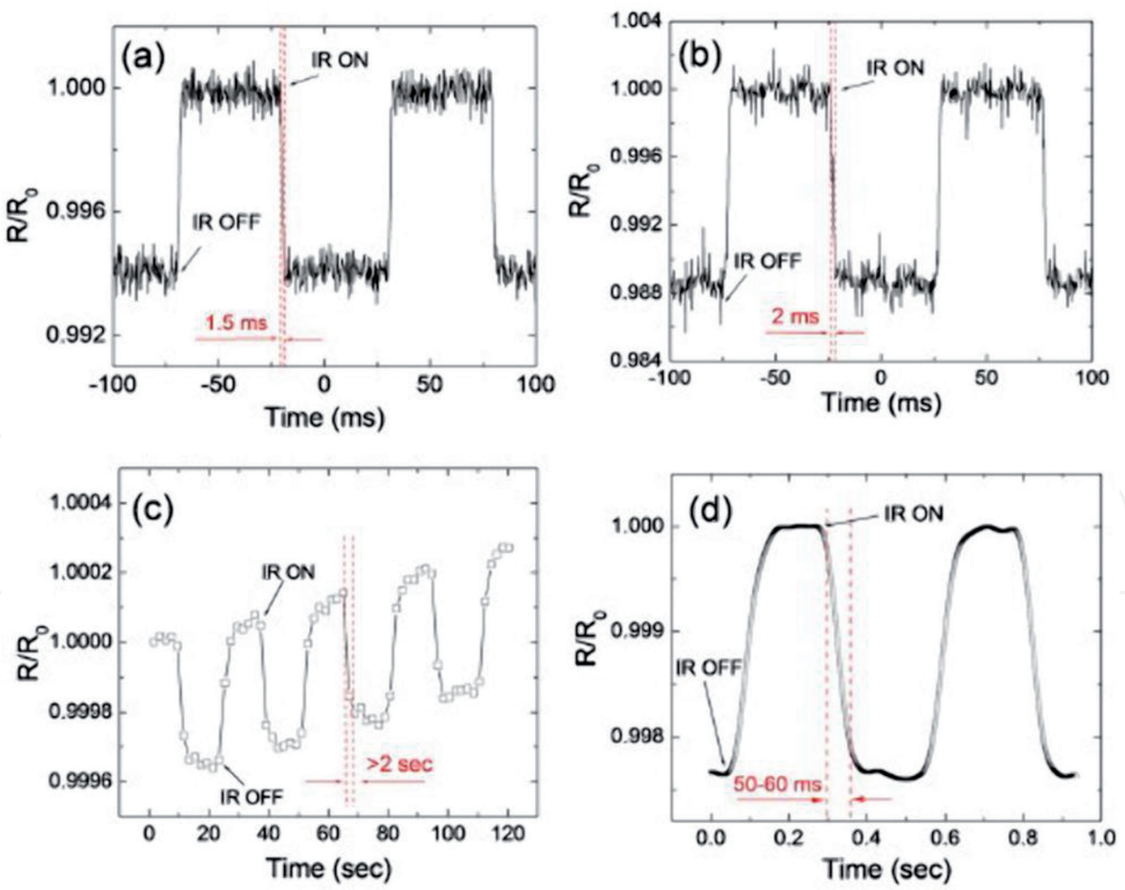

Figure 11.
Photoresponse of unsuspended and suspended CNT films. (a) Unsuspended MWCNT film (f = 10 Hz in IR, P = 3.0 mW/mm²); (b) suspended MWCNT film (f = 10 Hz in IR, P = 3.0 mW/mm²); (c) unsuspended SWCNT film (f = 1/30 Hz in IR, P = 3.5 mW/mm²); (d) suspended SWCNT film (f = 2 Hz in IR, P = 3.5 mW/mm²) [2].

technology we shall now discuss, though comprising an applied rather than a core component, has demonstrated the capability to extend and enhance the performance of a wide range of electro-optical and infrared systems and devices.

3. Nanostructured antireflection coatings for optical sensor applications

3.1 Overview of nanostructured AR coating technology

Reducing optical reflections from surfaces, which is important to many optical applications including optical lenses, windows, photovoltaic devices, and photodetectors, has commonly been achieved through coating, or texturing, the surfaces of interest. Nanostructures that minimize reflection loss have been investigated for the development of high performance antireflection (AR) coatings. Such nanostructured AR coatings having optimal index profiles can demonstrate broadband AR properties, particularly with air as the ambient medium.

Glass, a dielectric material widely used in a variety of optical applications including lenses, windows, and as a cover or encapsulation for semiconductor optoelectronic devices, is basically transparent to wavelengths longer than 400 nm. However, due to Fresnel reflection losses glass reflects about 4% of the incident light from its front surface, or ~8% from both surfaces. This undesired reflection in certain applications can degrade the efficiency of the underlying device (e.g., sensor or photovoltaic cell), reduce its signal-to-noise ratio (e.g., in the case of a photodetector), and cause glare (e.g., from electronic displays). For such applications, it is important not only to reduce reflectance but also to improve the transmittance through the surface. This requires that the coating material be nonabsorbent, and the coating surface be specular.

AR coatings have conventionally been composed of single layers having optical thicknesses equal to one quarter of the wavelength (λ/4) of interest. Ideally, such a single-layer λ/4 AR coating should have a refractive index $n_{\lambda/4}$ given by [18]:

$$n_{\lambda/4} \approx \sqrt{n_{substrate} \times n_{air}} \tag{10}$$

However, due to the unavailability of materials having the precise desired refractive index, the performance of λ/4 AR coatings often deviates from the optimum, which is especially the case for low-index substrates such as glass. For example, an ideal single-layer λ/4 AR coating on a glass surface in an air ambient would require a material with a refractive index of $(1.46)^{1/2} \approx 1.21$. Due to the unavailability of optical materials with very low ($n < 1.4$) refractive indexes, near-perfect graded-index AR coatings for glass substrates have not been practically achievable.

Recently, however, a new class of optical thin film materials consisting of tunable nanostructures has enabled the realization of very low refractive index materials [9, 19]. Using these nanostructured materials, AR coatings can greatly minimize reflection losses and enhance the sensitivity and performance of detection and imaging systems.

The multilayer AR coatings feature step-graded refractive indexes which decrease in discrete steps from that of the substrate (e.g., ~1.5 for SiO_2 or ~3.5 for Si) to a value of close to that of air (e.g., 1.18). These AR coatings with specular surfaces comprising multiple discrete layers of non-absorbing materials exploit thin film interference effects to reduce reflectance and maximize transmittance. Such discrete multilayer AR coatings, which have been shown outperform continuously-graded AR coatings, offer very effective antireflection performance [20].

Figure 12(a) shows the measured and calculated refractive index of deposited SiO_2 vs. deposition angle following a formula developed by Poxson et al. [20]. This plot demonstrates the potential to tune the refractive index of a given material to virtually any value between its bulk value and that of air (~1.0) through controlling the deposition angle. The SEM images in **Figure 12(b)** show the gradual decrease in density of SiO_2 nanocolumns transitioning from a dense bulk film deposited at an angle of 0° to a nanostructured film deposited at 75°.

3.2 Growth of nanostructured AR coating layers

The nanostructured optical layers are fabricated using a scalable physical vapor deposition (PVD) self-assembly process, which allows them to be processed on almost any type of substrate. This process involves the formation of a highly directional vapor flux, which can be implemented through melting various optical coating materials. Surface diffusion and self-shadowing effects during the growth process enable the formation of the nanostructured thin films.

As illustrated in **Figure 13**, random growth fluctuations on the substrate produce a shadow region that incident vapor flux cannot reach and a nonshadow region where incident flux deposits preferentially, creating rod-like structures with lower effective refractive indexes [21]. The deposition angle, the angle between the normal to the sample surface and the incident vapor flux, results in the formation of nanostructures tilted relative to the sample surface. This process offers advantages such as tunability of the refractive index, flexibility in choice of materials, simplicity of the growth process, and ability to optimize the coatings for any substrate-ambient material system.

Since the gaps between the nanostructures are typically much smaller than the wavelengths of visible and IR light, the nanostructured layer acts as a single homogenous film having a refractive index intermediate in value between that of the ambient air and of the nanostructure material that decreases in density with increasing gap size. Nanowires and other types of nanostructures grown by the self-assembly process provide a pathway for fabricating high-quality broadband AR coatings for a variety of nanosensor applications.

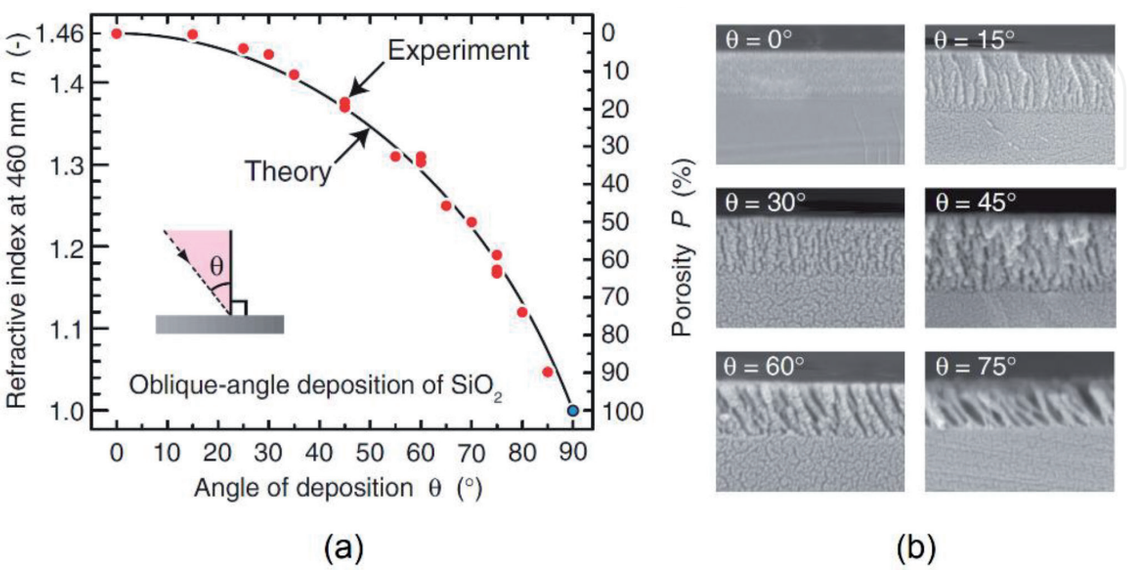

Figure 12.
(a) Refractive index of oblique-angle-deposited SiO_2 as a function of deposition angle. (b) SEM images showing a gradual decrease in density of SiO_2 nanocolumns for nanostructured AR coatings transitioning from a dense bulk film at 0° deposition angle to a nanostructured film at 75° deposition angle [20].

Figure 14 presents the measured refractive index dispersion curve as a function of wavelength from a nanostructured SiO_2 layer deposited at a highly oblique angle [22, 23]. This low-index nanostructured SiO_2 film was deposited on a Si substrate and measured by ellipsometry. Also shown is a comparison of experimental reflectivity data with theoretical calculations. These results illustrate that the nanostructures grown by the self-assembly process provide a pathway for fabricating high quality broadband AR coatings for a variety of sensing and imaging applications.

Figure 15 demonstrates the use of SiO_2 and TiO_2 nanostructures to achieve high performance, step-graded AR coatings on AlN substrates [10, 23]. In the following sections recent efforts are summarized to extend this technology to different substrates and lenses and to other bands of interest spanning the visible to the infrared for next-generation sensors.

3.3 Nanostructured AR coatings for visible EO applications

We have fabricated and tested various step-graded AR structures comprising layers of nanostructured SiO_2 using the PVD self-assembly process [17, 21, 24].

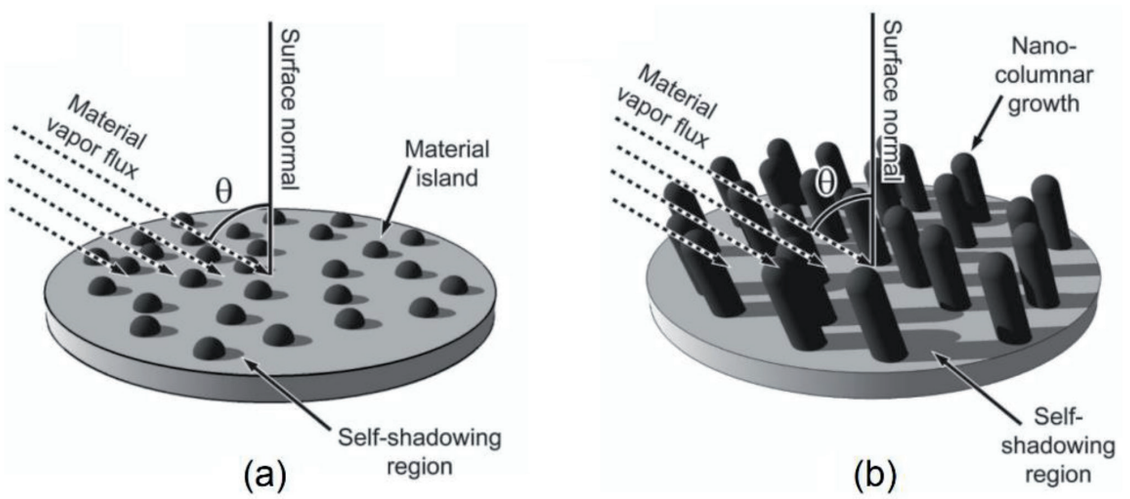

Figure 13.
(a) Schematic of self-assembly process for synthesis of nanostructured films, showing (a) initial formation of material islands at random locations across the substrate, followed by (b) formation of self-shadowed regions and nanocolumnar growth when the material vapor flux arrives at a non-normal deposition angle θ to the substrate [21].

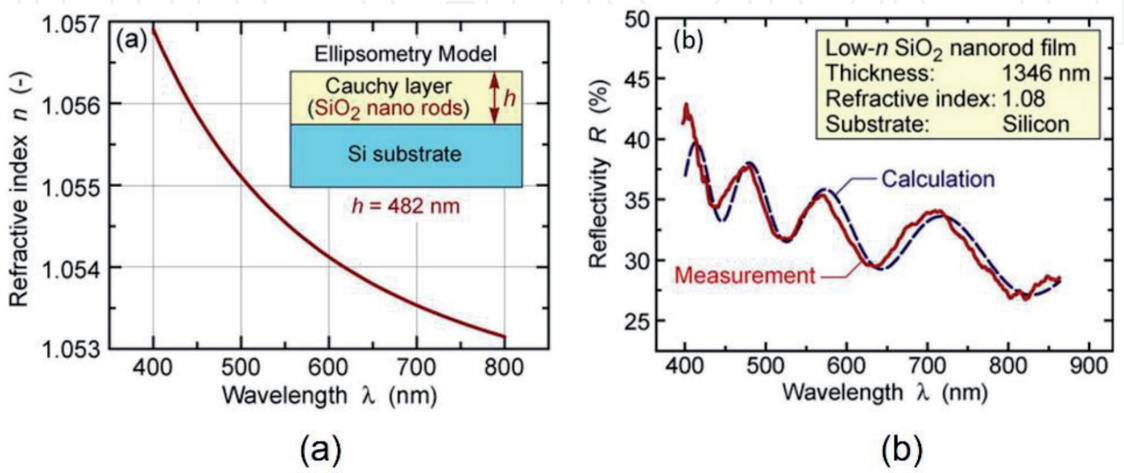

Figure 14.
(a) Refractive index dispersion curve of low-index SiO_2 nanostructure thin film on a Si substrate, with (b) comparison of the measured and calculated reflectivity spectra [22, 23].

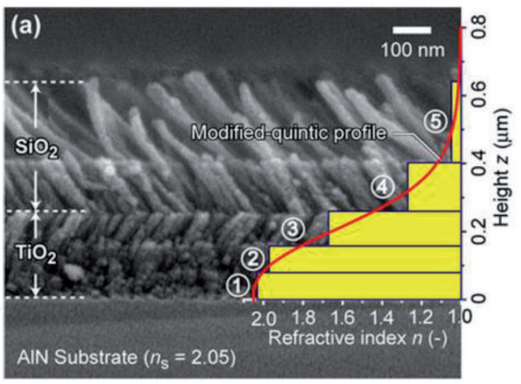

(b) Layer No.	1	2	3	4	5
Source	TiO_2			SiO_2	
Deposition angle	25°	40°	65°	–68°	–87°
Thickness (nm)	77.4	80.2	99.3	145.0	223.0
Refractive index, *n*	2.03	1.97	1.67	1.27	1.05

Figure 15.
(a) Cross-sectional SEM image of TiO_2 and SiO_2 step-graded index nanostructure coatings that approximate a modified quintic profile. The graded-index coating consists of three TiO_2 nanostructured layers and two SiO_2 nanostructured layers and (b) deposition angles, thicknesses, and refractive indexes for each layer in the graded index coating [10, 23].

These multilayer nanostructured AR coatings have been deposited on both sides of glass substrates, and the corresponding transmittance characterized as a function of wavelength and incident angle. The nanostructured AR coatings have likewise been successfully demonstrated on the curved surfaces of converging and diverging optical lenses, which are key components that manipulate the optical pathways in optical and infrared systems.

3.3.1 Glass substrates

Figure 16 compares the measured broadband performance of an uncoated glass slide to one coated on both sides with a multilayered, nanostructured SiO_2 coating, where the transmittance is characterized as a function of wavelength and light incidence angle [10]. The inset in **Figure 16** shows a representative cross-sectional SEM image of the two-layer structure. The nanostructured coatings were prepared in an electron beam evaporator using different deposition angles to form distinct layers with step-graded refractive index profiles.

The transmittances of the coated and uncoated glass slides were measured using an angle-dependent transmittance measurement setup consisting of a xenon lamp light source and Ando AQ6315A optical spectrum analyzer calibrated for detection of transmitted photons over the 400–800 nm wavelength range. The measured peak broadband transmittance at normal incidence of the uncoated glass slide was 92%, corresponding to ~4% reflection loss at each glass/air interface.

The peak transmittance was 98.3% for the double-sided, nanostructure-coated glass, implying an average broadband reflection loss of less than 1% at each glass/air interface. As shown in **Figure 16**, the transmittance through the nanostructured SiO_2 coated glass was also significantly higher than that through the uncoated glass across a wide range of incident angles. While the transmittance of the uncoated glass slide falls below 80% at an incident angle of 65°, the glass slide with the double-sided coating still maintains a transmittance above 95% at this angle of light incidence.

The transmittances of coated and uncoated glass slides have also been measured at normal incidence as functions of wavelength using a JASCO V-570 spectrophotometer. As shown in **Figure 17**, the average measured broadband transmittance between 350 nm and 1800 nm increases from 92.2% for the uncoated glass to 98.6% for the double-sided nanostructured coated glass [9]. This transmittance exceeds 97.8% at all wavelengths between 440 and 1800 nm, corresponding to a glass-air

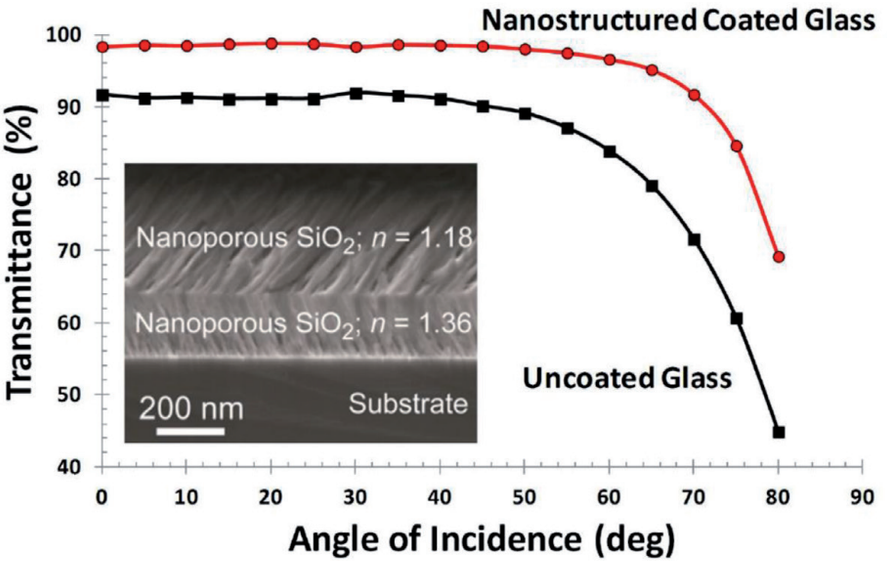

Figure 16.
Incident angle dependent broadband transmittance through glass slide coated on both sides with a step-graded, nanostructured SiO_2 AR coating, along with that for an uncoated glass slide. A representative cross-sectional SEM image of the dual-layer nanostructured coating is shown in the inset [10].

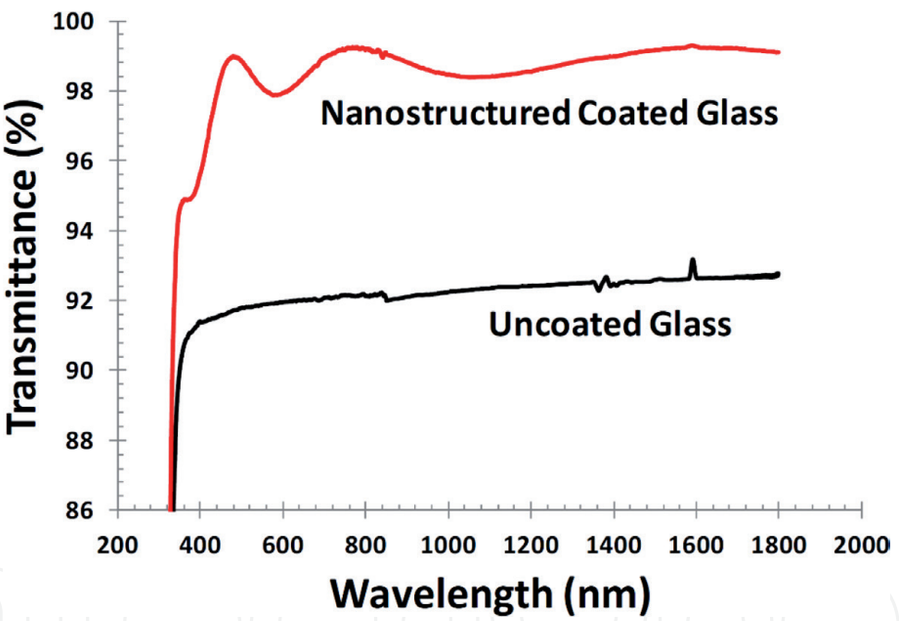

Figure 17.
Wavelength-dependent transmittance measurement of step-graded, nanostructured SiO_2 AR coating on glass substrate [9].

interface reflectivity below 1.1% over this relatively wide spectrum. These optimized nanostructured AR coatings have been shown to outperform ideal quarter-wavelength MgF_2 coatings over all visible wavelengths and incident angles [21].

3.3.2 Optical lenses

Light passing through an uncoated lens will suffer reflection losses at both the input and output lens interfaces. These losses add up and can limit the performance of detector devices. Demonstration of AR coatings on curved lens surfaces extends their benefits for optical system applications.

We have designed and optimized step-graded index profiles for optical lenses, as well as for ZnSe IR lenses which are covered in the following section. Multilayer

step-graded AR coating index profiles were created and optimized for glass lenses by controlling the refractive index profiles and thicknesses of the individual layers. Nanostructured SiO_2 layers of the desired refractive index were deposited on the entire surface of the optical lens by the self-assembly process. **Figure 18** compares the transmittance of uncoated and nanostructured SiO_2 multilayer AR-coated optical lenses [10].

The nanostructured AR coating significantly improves the optical transmittance through the lens from 94% to nearly 100%, which is maintained over the entire visible and majority of the NIR spectra. AR-coated lenses can thus transmit a virtually unattenuated optical signal to a sensor over a broader spectrum through eliminating unwanted reflections, enabling more effective detector devices with significantly higher responsivities. This approach can be expanded to benefit various IR components, significantly improving the detection, sensing, and imaging capabilities of electro-optical and infrared systems.

3.3.3 Flexible substrates

Broadband and high-performance AR coatings have been demonstrated on flexible substrates such as polycarbonate films. Polycarbonate is a useful material for commercial products including display filters, plastic lenses, and face shields, and is commonly utilized for defense applications as well. Polycarbonate also provides high impact resistance and has an excellent flammability rating.

Nanostructured multilayer SiO_2 AR coatings having optimized step-graded index profiles have been deposited on both sides of polycarbonate sheets. **Figure 19** compares the optical transmittance spectra of uncoated and AR-coated polycarbonate sheets [9]. The expanded transmittance spectrum over the visible (~400–800 nm) band is plotted in the inset of **Figure 19**. As seen in the inset, the uncoated polycarbonate sheet shows approximately 90% transmittance over the visible spectrum. For the AR-coated polycarbonate sheet, however, the transmittance rises to nearly 100%, and this enhancement is observed for the entire visible and part of the NIR band. Such high AR performance demonstrated over the entire visible spectrum makes the nanostructure AR coatings potentially beneficial for certain electro-optical applications including CMOS image sensors.

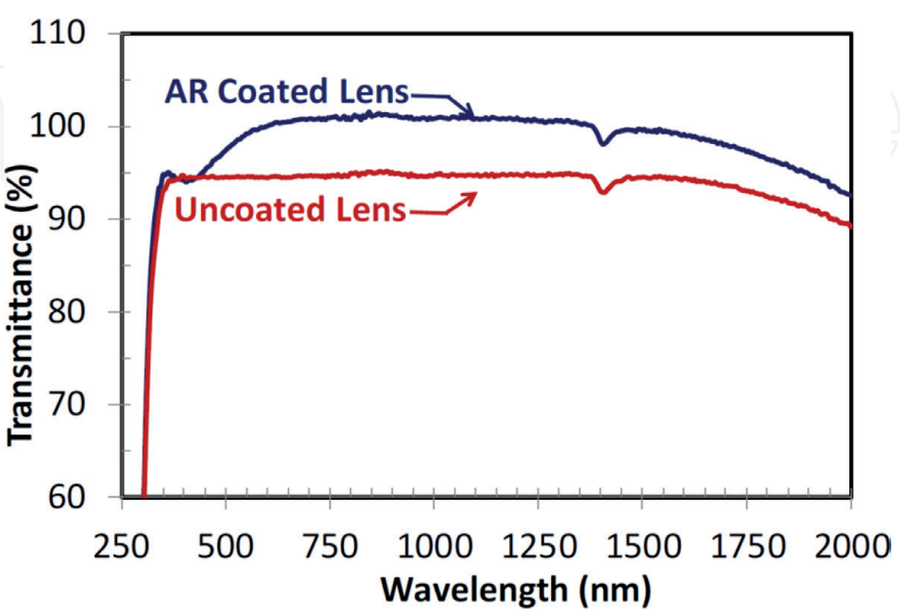

Figure 18.
Measured wavelength-dependent transmittance of nanostructured SiO_2 coated lens compared to an uncoated lens. The AR coating provides nearly 100% transmittance, which is maintained over a wide spectrum of light [10].

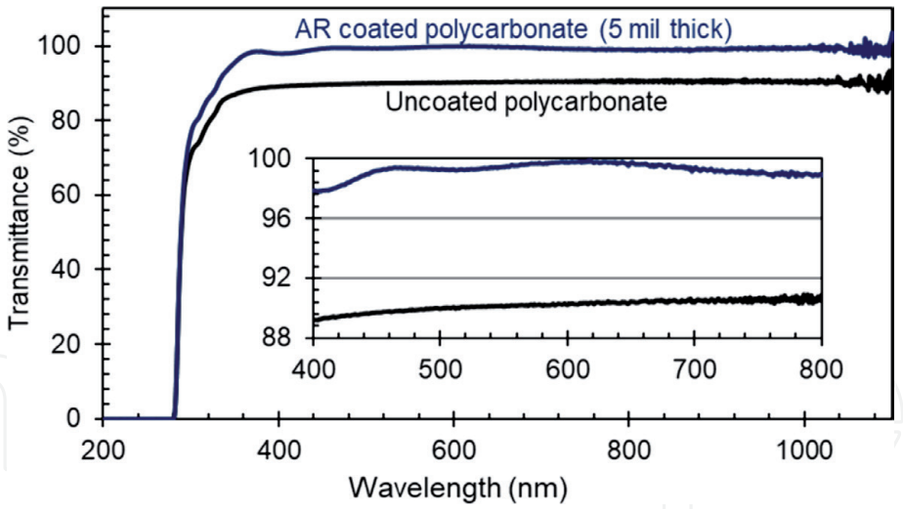

Figure 19.
Optical transmittance spectrum of transparent polycarbonate film (5 mil thickness) before and after application of nanostructured AR coating. The AR coating provides nearly 100% transmittance at 610 nm [9].

3.4 IR applications of nanostructured AR coatings

Infrared detection technology plays a critical role in various terrestrial and space applications. In order to extend the application of the AR coatings to MWIR and LWIR spectral bands, nanostructured AR coatings have been fabricated on silicon wafers by sequentially growing multiple nanostructured Si and SiO_2 layers with desired graded-index profiles through control of the deposition angle. These AR coatings minimize the reflection loss from approximately 30% to less than 1.5% over IR bands.

3.4.1 MWIR applications

The measured wavelength-dependent reflectance of multilayer AR-coated and uncoated Si substrates are shown plotted in **Figure 20** [9]. The multilayer AR coating has been synthesized with graded-index profiles optimized for the 3–5 μm MWIR band. As seen in the figure, the average measured reflectance for the multilayer AR-coated Si wafer is less than 1.5%, while the average measured reflectance for the uncoated silicon <211> wafer is ~35% over the 3–5 μm MWIR spectral band.

3.4.2 LWIR applications

The measured wavelength-dependent reflectance of an uncoated Si substrate and AR-coated Si <211> substrate having an index profile specifically designed for the 6–11 μm LWIR spectral band is plotted in **Figure 21** [25]. This dual-layer AR coating was synthesized by sequentially growing two nanostructured Si layers each at different deposition angles.

The average reflectance from 6 to 11 μm for the two-layer AR-coated Si wafer is less than 1.5%, while that of the uncoated Si <211> wafer is ~28%. These results clearly demonstrate that the multilayer AR coating significantly minimizes incident IR signal losses over the LWIR band.

Infrared optical components such as windows and lenses typically reflect a significant portion of the incoming IR signal to be detected. The incorporation of AR coatings on these IR components can greatly enhance overall system performance. We have demonstrated the nanostructured AR coatings on various components for improved IR performance, including ZnSe lenses for LWIR applications.

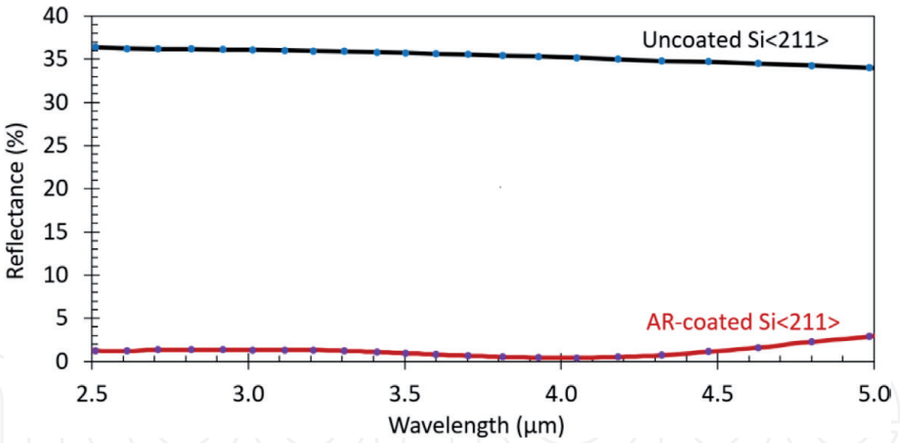

Figure 20.
Measured wavelength-dependent reflectance of multilayer AR-coated and uncoated Si <211> wafers. The multilayer AR coating on Si <211> wafers offers significantly lower reflectance over the 3–5 μm MWIR spectral band [9].

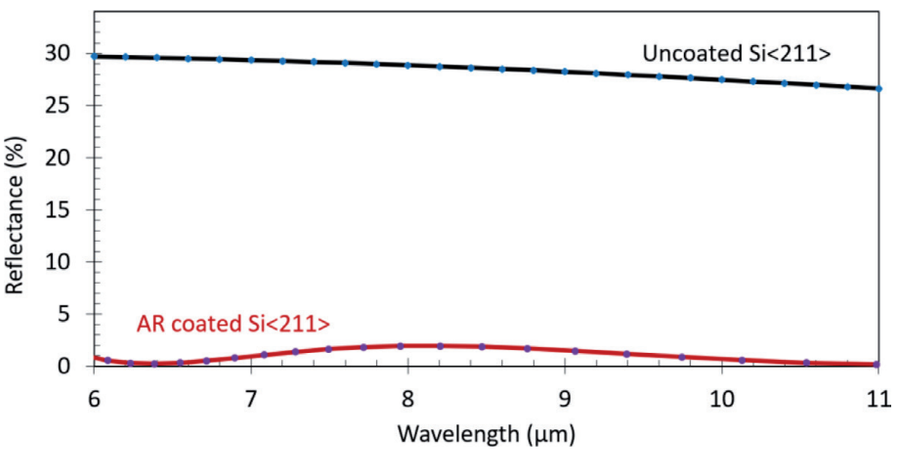

Figure 21.
Measured LWIR wavelength-dependent reflectance of two-layer AR coating structure on Si <211> substrate with that for an uncoated substrate. The AR coating significantly reduces reflection over this range compared to the uncoated Si substrate [25].

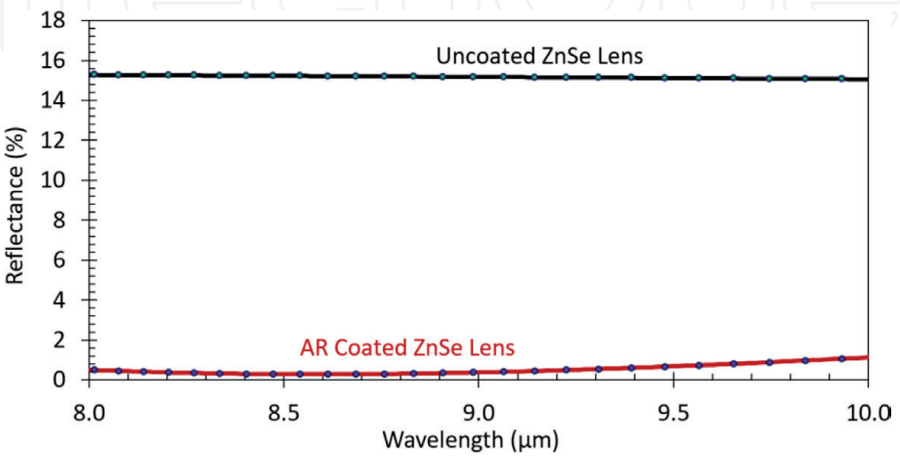

Figure 22.
Measured wavelength-dependent reflectance of uncoated and single-layer nanostructure AR-coated ZnSe lenses. The AR-coated ZnSe lens demonstrates an average reflectance of 0.6%, compared to 15.2% for the uncoated ZnSe lens, over the 8–10 μm spectral band [9].

Single-layer nanostructured AR coatings have been applied to ZnSe lenses that significantly enhance performance by minimizing the reflection of incident IR signals at the lens surfaces. **Figure 22** compares the measured reflectance spectra of ZnSe lenses with and without the AR coatings [9]. The AR-coated ZnSe lens reflects on average ~0.6% of the incident signal over the 8–10 μm band, compared to reflectance of ~15% for the uncoated lens. The performance of the nanostructured AR coatings may be further improved by implementing multilayer rather than single-layer structures.

4. Summary and conclusions

In this chapter we have first discussed recent efforts towards the design, modeling, and experimental development of next-generation carbon nanotube-based bolometers for IR sensing and imaging. The goal in the development and advancement of this technology is to enable high performance, high frame rate, uncooled microbolometers for MWIR and LWIR bands. We have presented recent results of growing variously orientated SWCNT and MWCNT films that demonstrate the promise of using CNTs for developing high performance and small pixel microbolometer arrays.

The growth and application of nanostructured layers for developing high quality antireflection coatings likewise offers an innovative approach for minimizing reflection losses in state-of-the-art sensors and optical windows for both defense and commercial applications. The step-graded multilayer antireflection technology has been shown to be both broadband and omnidirectional in nature. These nanostructure-based AR coatings have demonstrated high performance over spectral bands spanning the visible to the IR with the potential to include larger area substrates to benefit next-generation sensors.

Optical sensing technology is critical for various defense and commercial applications including optical communication and IR imaging. Advances in detector materials and technologies have been achieved over a broad spectrum using Si and SiO_2 based nanostructures and novel carbon nanotube-based materials. These technological advances are opening doors for new approaches to apply device design methodologies that can offer enhanced performance and low-cost optical sensors and systems benefitting a wide range of infrared and electro-optical applications.

Acknowledgements

The authors thank Dr. Whitney Mason of DARPA/MTO for technical discussions and guidance. We would like to thank Ms. Susan Celis and Mr. Oscar Cerna of DARPA for their ongoing support. This research was developed with Phase II SBIR Programs from the Defense Advanced Research Projects Agency (DARPA) and the Army Research Laboratory (ARL). The views, opinions and/or findings expressed are those of the author and should not be interpreted as representing the official views or policies of the Department of Defense or the U.S. Government. Distribution Statement "A" (Approved for Public Release, Distribution Unlimited).

Author details

Ashok K. Sood[1], John W. Zeller[1*], Gopal G. Pethuraja[1], Roger E. Welser[1], Nibir K. Dhar[2] and Priyalal S. Wijewarnasuriya[3]

1 Magnolia Optical Technologies, Inc., Woburn, MA, USA

2 U.S. Army Night Vision and Electronic Sensors Directorate, Fort Belvoir, VA, USA

3 U.S. Army Research Laboratory, Adelphi, MD, USA

*Address all correspondence to: jwzeller@magnoliaoptical.com

References

[1] Sood AK, Richwine RA, Puri YR, Dhar NK, Polla DL, Wijewarnasuriya PS. Multispectral EO/IR sensor model for evaluating UV, visible, SWIR, MWIR and LWIR system performance. In: Proceedings of SPIE; 1 May 2009; Orlando. Bellingham: SPIE; 2009. p. 73000H

[2] Sood AK, Zeller JW, Welser RE, Puri YR, Lewis JS, Dhar NK, et al. Overview of detector technologies for EO/IR sensing applications. In: Proceedings of SPIE; 26 May 2016; Baltimore. Bellingham: SPIE; 2016. p. 98540A

[3] Dhar NK, Dat R, Sood AK. Advances in infrared detector array technology. In: Pyshkin SL, Ballato JM, editors. Optoelectronics: Advanced Materials and Devices. London: IntechOpen; 2013. pp. 149-190. DOI: 10.5772/51665

[4] Sood AK, Puri YR, Dhar NK, Polla DL. Recent advances in EO/IR imaging detector and sensor applications. In: Vaccca JR, editor. Handbook of Sensor Networking: Advanced Technologies and Applications. 1st ed. Boca Raton: CRC Press; 2015. pp. 18-21. DOI: 10.1201/b18001-5

[5] Sood AK, Lund I, Puri YR, Efstathiadis H, Haldar P, Dhar NK, et al. Review of graphene technology and its applications for electronic devices. In: Ebrahimi F, editor. Graphene: New Trends and Developments. London: IntechOpen; 2015. pp. 59-89. DOI: 10.5772/61316

[6] Sood A. K, Lund I, Zeller J. W, Puri Y. R, Efstathiadis H, Haldar P, et al. Development of graphene based detectors for EO/IR applications. In: Proceedings of SPIE; 26 May 2016; Baltimore. Bellingham: SPIE; 2016. p. 98540D

[7] Fernandes GE, Kim JH, Xu J, Sood AK, Dhar NK, Dubey M. Unleashing giant TCR from phase changes in carbon nanotube composites. In: Proceedings of SPIE; 19 September 2013; Baltimore. Bellingham: SPIE; 2013. p. 88680S

[8] Fernandes GE, Kim JH, Sood AK, Xu J. Giant temperature coefficient of resistance in carbon nanotube/phase-change polymer nanocomposites. Advanced Functional Materials. 2013;**23**:4678-4683. DOI: 10.1002/adfm.201300208

[9] Pethuraja GG, Zeller JW, Welser RE, Sood AK, Efstathiadis H, Wijewarnasuriya PS. Nanostructured antireflection coatings for infrared sensors and applications. In: Proceedings of SPIE; 18 September 2018; San Diego. Bellingham: SPIE; 2018. p. 107660I

[10] Pethuraja GG, Zeller JW, Welser RE, Sood AK, Efstathiadis H, Haldar P, et al. Development of nanostructured antireflection coatings for electro-optic infrared technologies. Sensors & Transducers Journal. 2017;**214**:46-52

[11] Jariwala D, Srivastava A, Ajayan P. Graphene synthesis and band gap opening. Journal of Nanoscience and Nanotechnology. 2011;**11**:6621-6641. DOI: 10.1166/jnn.2011.5001

[12] Sood AK, Lund I, Puri YR, Efstathiadis H, Haldar P, Dhar NK, et al. A review of growth, functionalization, and use of graphene for detection applications. International Journal of Nanoscience and Nanotechnology. 2014;**5**:133-150

[13] Sood AK, Egerton EJ, Puri YR, Fernandes G, Xu J, Akturk A, et al. Design and development of carbon nanotube-based microbolometer for IR imaging applications. In: Proceedings of SPIE; 31 May 2012; Baltimore. Bellingham: SPIE; 2012. p. 83533A

[14] Tîlmaciu CM, Morris MC. Carbon nanotube biosensors. Frontiers in Chemistry. 2015;**59**:1-21. DOI: 10.3389/fchem.2015.00059

[15] Razeghi M. Current status and future trends of infrared detectors. Opto-Electronics Review. 1998;**6**:155-194

[16] Sood AK, Egerton JE, Puri YR, Fernandes G, Kim JH, Xu J, et al. Carbon nanotube based microbolometer development for IR imager and sensor applications. In: Proceedings of SPIE; 16 September 2011; San Diego. Bellingham: SPIE; 2011. p. 815513

[17] Sood AK, Welser RE, Puri YR, Dhar NK, Polla DL, Wijewarnasuriya P, et al. Nanostructured detector technologies for optical sensing applications. In: Proceedings of SPIE; 4 June 2014; Baltimore. Bellingham: SPIE; 2014. p. 91000N

[18] Sood AK, Welser RE, Pethuraja GG, Sood AW, Puri YR, Shubert EF, et al. Nanostructured antireflection (AR) coatings of optoelectronic applications. In: Aliofkhazraei M, editor. Comprehensive Guide for Nanocoatings Technology. Vol. 4. Hauppauge: Nova Science Publishers; 2015. pp. 183-216

[19] Pethuraja GG, Welser RE, Zeller JW, Puri YR, Sood AK, Efstathiadis H, et al. Nanostructured antireflection coatings for optical detection and sensing applications. In: MRS Proceedings; 10 July 2015; San Francisco. Warrendale: MRS; 2015. p. mrss15-2137947

[20] Chhajed S, Poxson DJ, Yan X, Cho J, Schubert EF, Welser RE, et al. Nanostructured multilayer tailored-refractive-index antireflection coating for glass with broadband and omnidirectional characteristics. Applied Physics Express. 2011;**4**:052503. DOI: 10.1143/apex.4.052503

[21] Welser RE, Sood AW, Pethuraja GG, Sood AK, Yan X, Poxson DJ, et al. Broadband nanostructured antireflection coating on glass for photovoltaic applications. In: Proceedings of the 38th IEEE Photovoltaic Specialists Conference; 3-8 June 2012; Austin. New York: IEEE; 2012. pp. 003339-003342

[22] Xi JQ, Schubert MF, Kim JK, Schubert EF, Chen M, Lin SY, et al. Optical thin-film materials with low refractive index for broadband elimination of Fresnel reflection. Nature Photonics. 2007;**1**:176-179. DOI: 10.1038/nphoton.2007.26

[23] Pethuraja GG, Zeller JW, Welser RE, Efstathiadis H, Haldar P, Wijewarnasuriya PS, et al. Development of nanostructured antireflection coatings for infrared technologies and applications. In: Proceedings of SPIE; 19 September 2017; San Diego. Bellingham: SPIE; 2017. p. 104040S

[24] Sood A K, Pethuraja G, Welser R. E, Puri Y. R, Dhar N. K, Wijewarnasuriya P. S, et al. Development of large area nanostructured antireflection coatings for EO/IR sensor applications. In: Proceedings of SPIE; 28 August 2015; San Diego. Bellingham: SPIE; 2015. p. 96090D

[25] Pethuraja GG, Zeller JW, Welser RE, Sood AK, Efstathiadis H, Wijewarnasuriya P. Nanostructured antireflection coatings for infrared sensors and applications. In: Proceedings of the 2018 U.S. Workshop on the Physics and Chemistry of II-VI Materials; 22-25 October 2018; Pasadena. New York: Palisades; 2018. p. 117